



# Host–guest complexation-mediated codelivery of anticancer drug and photosensitizer for cancer photochemotherapy

Guocan Yu<sup>a,1</sup>, Benyue Zhu<sup>b,1</sup>, Li Shao<sup>c,1</sup>, Jiong Zhou<sup>c,1</sup>, Manik Lal Saha<sup>d</sup>, Bingbing Shi<sup>d</sup>, Zibin Zhang<sup>b</sup>, Tao Hong<sup>b</sup>, Shijun Li<sup>b,2</sup>, Xiaoyuan Chen<sup>a,2</sup>, and Peter J. Stang<sup>d,2</sup>

<sup>a</sup>Laboratory of Molecular Imaging and Nanomedicine, National Institute of Biomedical Imaging and Bioengineering, National Institutes of Health, Bethesda, MD 20892; <sup>b</sup>College of Material, Chemistry and Chemical Engineering, Hangzhou Normal University, 311121 Hangzhou, P. R. China; <sup>c</sup>State Key Laboratory of Chemical Engineering, Center for Chemistry of High-Performance & Novel Materials, Department of Chemistry, Zhejiang University, 310027 Hangzhou, P. R. China; and <sup>d</sup>Department of Chemistry, University of Utah, Salt Lake City, UT 84112

Contributed by Peter J. Stang, February 13, 2019 (sent for review February 5, 2019; reviewed by Jean-Marie P. Lehn and Vivian Wing-Wah Yam)

Although platinum-based anticancer drugs prevail in cancer treatment, their clinical applications are limited by the severe side effects as well as their ineffectiveness against drug resistant cancers. A precise combination of photodynamic therapy (PDT) and chemotherapy can synergistically improve the therapeutic outcome and thereby may overcome drug resistance through a multipronged assault. Herein, we employ the well-defined cavity of a discrete organoplatinum(II) metallacage (M) to encapsulate octaethylporphine (OEP), a photosensitizer, forming a dual-functionalized system M⊃OEP that is wrapped into the hydrophobic core of the nanoparticles (MNPs) self-assembled from an amphiphilic diblock copolymer. Using a copper-free click reaction, a targeting ligand is conjugated on the surface of the MNPs, aiming to specifically deliver a chemotherapeutic drug and a photosensitizer to cancer cells. Benefiting from the enhanced permeability and retention effect and active targeting capability, high tumor accumulation of MNPs is achieved, leading to an improved therapeutic outcome and reduced side effects. In vivo studies demonstrate that the combination of chemotherapy and PDT exhibits a superior antitumor performance against a drug-resistant tumor model attributed to their synergistic anticancer efficacy.

supramolecular coordination complex | metallacage | photodynamic therapy | theranostic | drug delivery

Platinum-based drugs including cisplatin, carboplatin, and oxaliplatin are used worldwide in cancer treatment; however, their dose-limiting side effects arising from the poor selectivity to cancerous tissue over normal tissues always cause serious complications in patients (1–5). Considerable attention has been given to the development of smart drug-delivery systems that can temporarily passivate platinum complexes and specifically transport the nanomedicines to tumor sites via the enhanced permeability and retention (EPR) effect (6–8). Various nanocarriers including liposomes, micelles, and dendrimers have been employed that can selectively transport platinum-based anticancer drugs to cancerous cells (9–11), while the clinical use of these nanomedicines is still limited by drug resistance, including inherent and acquired resistance, promoting researchers to combine chemotherapy with other treatment modalities to achieve synergetic anticancer efficacy through a multipronged assault (12–15).

Photodynamic therapy (PDT) employs photosensitizers that upon absorbing a specific wavelength of light to release a cell-damaging version of reactive oxygen species (singlet oxygen, <sup>1</sup>O<sub>2</sub>) that can eradicate tumors with a high specificity and negligible side effects (16–18). The sensitization effect of PDT can significantly boost the activity of chemotherapeutic agents, synergistically overcoming drug resistance through different mechanisms of actions to realize enhanced anticancer efficacy (19–22). However, the full promise of PDT has not yet been achieved mainly due to the lack of ideal photosensitizers and sophisticated delivery/activation processes. Many existing photosensitizers, such as phthalocyanine, porphyrin,

bacteriochlorin derivatives, and boron dipyrromethene dyes, are conjugated molecules with poor water solubility and exhibit serious aggregation tendency under physiological conditions, both of which lower the PDT efficacy (23, 24). Moreover, the suboptimal tumor accumulation of the photosensitizers after systemic administration also reduces the efficacy of PDT in clinical use.

To overcome these issues, we utilize a discrete organoplatinum(II) metallacage (M) to complex a photosensitizer [octaethylporphine (OEP)] through noncovalent interactions (Fig. 1). *Cis*-(PEt<sub>3</sub>)<sub>2</sub>Pt(OTf)<sub>2</sub> (cPt), a chemotherapeutic agent, is employed as the corners of the metallacage such that the host–guest complex M⊃OEP can act as a dual functionalized system to achieve synergistic anticancer efficacy. The solubility and stability of M⊃OEP in a physiological environment are improved by wrapping it into the hydrophobic core of an amphiphilic diblock copolymer (N<sub>3</sub>-PEG-*b*-PLBG), resulting in the formation of nanoparticles (MNPs) having azide groups on the surface for further incorporating a targeting ligand (cRGDfK) via an in situ

## Significance

The combination of chemotherapy and photodynamic therapy opens up a promising way of overcoming drug resistance, incorporating different mechanisms of actions to achieve synergistic efficacy. However, the antitumor outcome of photodynamic therapy is greatly limited due to the unsatisfactory singlet oxygen generation caused by severe aggregation of the photosensitizer. To this end, we utilize a discrete metallacage containing therapeutic organoplatinum(II) to encapsulate a photosensitizer by forming an inclusion host–guest complex, facilitating the codelivery of chemotherapeutic agent and photosensitizer through nanoformulation. Benefiting from the enhanced permeability and retention effect and active targeting, the nanomedicine exhibits satisfactory antitumor performance against drug-resistant tumor. This pioneering work provides a distinct supramolecular methodology to prepare theranostic systems for multimodality imaging and therapy.

Author contributions: G.Y., S.L., X.C., and P.J.S. designed research; B.Z., L.S., J.Z., B.S., Z.Z., and T.H. studied the host–guest investigations; G.Y., L.S., and J.Z. conducted the in vitro and in vivo studies; G.Y., M.L.S., S.L., X.C., and P.J.S. analyzed data; and G.Y., M.L.S., S.L., X.C., and P.J.S. wrote the paper.

Reviewers: J.-M.P.L., Université Louis Pasteur–Institut de Science et d’Ingénierie Supramoléculaires; and V.W.-W.Y., The University of Hong Kong.

The authors declare no conflict of interest.

Published under the PNAS license.

<sup>1</sup>G.Y., B.Z., L.S., and J.Z. contributed equally to this work.

<sup>2</sup>To whom correspondence may be addressed. Email: L\_shijun@hznu.edu.cn, shawn.chen@nih.gov, or stang@chem.utah.edu.

This article contains supporting information online at [www.pnas.org/lookup/suppl/doi:10.1073/pnas.1902029116/-DCSupplemental](http://www.pnas.org/lookup/suppl/doi:10.1073/pnas.1902029116/-DCSupplemental).

Published online March 20, 2019.

copper-free click reaction. Benefiting from these rational designs, high tumor accumulation and cellular internalization of **MNPs** are realized, which are beneficial to improve the therapeutic results while reducing the systemic toxicity. In vivo studies demonstrate that **MNPs** hold superior anticancer ability to overcome drug resistance, effectively suppressing tumor growth by combining chemotherapy and PDT.

## Results and Discussion

Using a multicomponent coordination self-assembly approach, **M** was quantitatively prepared from a total of 20 molecular components from three unique species, including hexakis[4-(4-pyridylethynyl)phenyl]benzene (**HPPB**), disodium terephthalate (**DSTP**), and **cPt**, in a 2:6:12 ratio, respectively (Fig. 1A). The successful construction of **M** was verified by  $^1\text{H}$  NMR and  $^{31}\text{P}\{^1\text{H}\}$  NMR spectroscopies. Well-defined signals were observed for the protons of **M** in the  $^1\text{H}$  NMR spectrum (SI Appendix, Fig. S3), suggesting that the resultant species possessed a discrete and highly symmetric structure (25–28). Compared with free **HPPB**, the  $^1\text{H}$  NMR signals related to the pyridyl protons ( $\text{H}_1$  and  $\text{H}_2$ ) shifted downfield upon formation of **M** due to the  $\text{Pt(II)}\leftarrow$ pyridine coordination interactions (SI Appendix, Fig. S3), while the peaks corresponding to the protons  $\text{H}_3$  and  $\text{H}_4$  shifted upfield. Attributed to the heterologation-directed coordinations between  $\text{Pt(II)}\leftarrow$ pyridine and  $\text{Pt(II)}\leftarrow$ carboxylate, the single peak of **cPt** in  $^{31}\text{P}\{^1\text{H}\}$  spectrum split into two different doublets after coordination (Fig. 2A and B), further confirming the putative structure of a discrete metallacage.

The host–guest complexation between **M** and **OEP** was confirmed by the  $^{31}\text{P}\{^1\text{H}\}$  spectrum, in which significant downfield shifts (from 5.13 and  $-0.33$  ppm to 8.49 and 3.03 ppm, respectively) were observed after the addition of **OEP** into the solution of **M** (Fig. 2C). Additionally, the host–guest interactions were examined by molecular modeling,  $^1\text{H}$  NMR, ultraviolet and visible (UV-vis), and fluorescence spectroscopies (SI Appendix,

Figs. S4–S8). From the  $^1\text{H}$  NMR titration data, the association constant was calculated to be  $(4.91 \pm 0.36) \times 10^4 \text{ M}^{-1}$  with a 1:1 stoichiometry using a nonlinear curve-fitting method (SI Appendix, Figs. S9–S12). Transmission electron microscopy (TEM) and scanning electron microscopy (SEM) demonstrated that free **OEP** molecules could stack into the nanofibers that were transformed into irregular aggregates in aqueous solution upon addition of **M** (SI Appendix, Fig. S13). These studies revealed that the  $\pi$ - $\pi$  stacking interactions among the free **OEP** molecules were greatly inhibited after the host–guest complexation, indicating that the photosensitizer could be well dispersed via the supramolecular strategy.

For biomedical applications, the stability and solubility of **M** and **OEP** need to be further improved. Hence, **N<sub>3</sub>-PEG-*b*-PLBG** was utilized as a polymeric shield that encapsulated **M** and **OEP** into its hydrophobic core and provided **MNPs** consisting of 30.6% **M** and **OEP** (SI Appendix, Table S1). To endow the nanoparticles with a targeting capability toward the  $\alpha_v\beta_3$  integrin overexpressing cancer cells, cyclic RGD (cRGDfK) functionality was attached on the surface of **MNPs** via a copper-free click reaction between cRGDfK-DBCO and the azide groups of the polymeric shield. The resultant functionalized nanoparticles were characterized by a suite of analytical techniques. For example, dynamic light scattering (DLS) measurement indicated that the average diameter of **MNPs** was  $109 \pm 8.4 \text{ nm}$  (SI Appendix, Figs. S14 and S15), which was in accordance with their TEM data (Fig. 3A). The zeta potential of **MNPs** was determined to be  $3.45 \pm 0.21 \text{ mV}$  (SI Appendix, Fig. S16). DLS was further employed to examine the stability of **MNPs** in a physiologic environment, the results showed a negligible change in the average diameter of **MNPs** even after its incubation in PBS containing 10% FBS for over 72 h (SI Appendix, Fig. S17). The PEG segments in **MNPs** likely provided a neutral shell to inhibit the absorption by proteins during the delivery process (29, 30).

The release behaviors of **cPt** and **OEP** from the **MNPs** were studied using inductively coupled plasma mass spectrometry (ICP-MS) and UV-vis spectroscopy under different conditions.

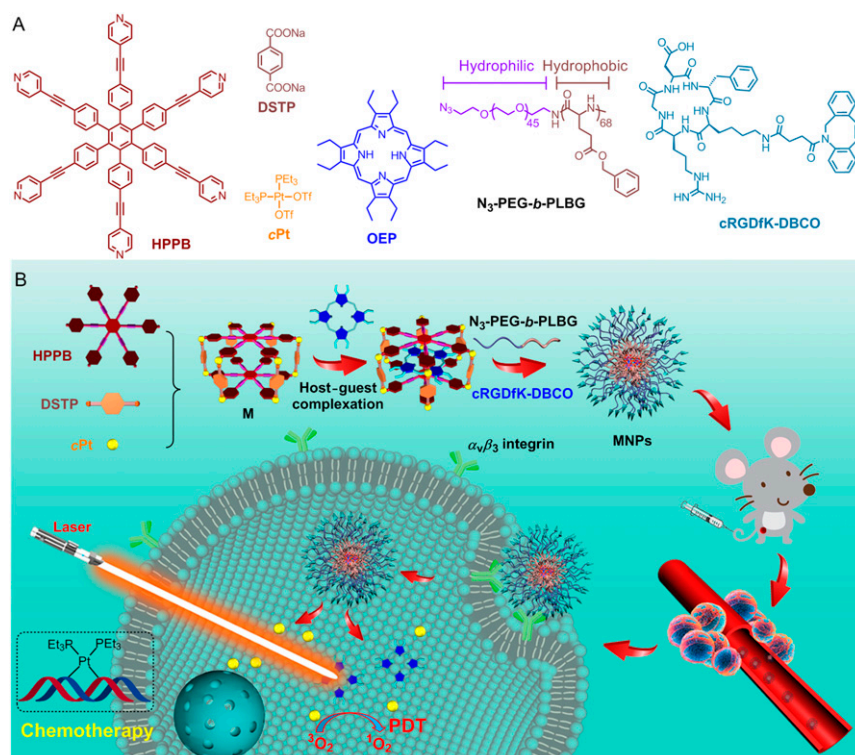


**Fig. 1.** (A) Chemical structures of **HPPB**, **DSTP**, **cPt**, **OEP**, **N<sub>3</sub>-PEG-*b*-PLBG**, and **cRGDfK-DBCO**. (B) Cartoon illustration of the preparation of **MNPs** and their photochemotherapy, followed by the tumor accumulation through EPR effect and receptor-mediated internalization.

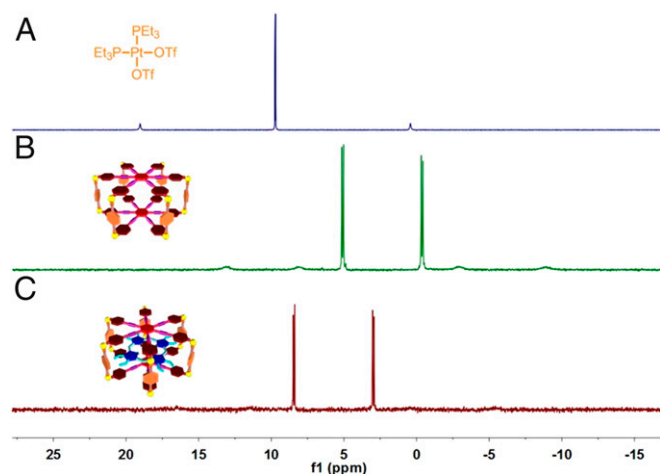


**Fig. 2.**  $^{31}\text{P}\{^1\text{H}\}$  NMR spectra (121.4 MHz,  $\text{CD}_2\text{Cl}_2/\text{CD}_3\text{CN} = 1/1$ , 298 K) of **cPt** (A), **M** (B), and **M $\Delta$ OEP** (C).

As illustrated in Fig. 3C, the release curve depicted a slow and sustained manner at pH 7.4, with a plateau of a total of 20.5% platinum released over 48 h, indicating that these **MNPs** were fairly stable under physiological conditions. The release was accelerated at pH 5.5, likely due to the dissociation of the metallacages under acidic condition by protonating the pyridine and carboxylate groups, which was beneficial for drug release after being internalized by cancer cells. A substantially faster and more profound release of **cPt** was observed when the **MNPs** were incubated in the presence of GTP at pH 5.5, in which ca. 96% of **cPt** was released from the **MNPs** within 48 h. This likely indicated that the coordination interactions between the  $\text{N}_7$  atoms of guanosine and the platinum centers facilitated the dissociation of the metallacage (31, 32). **OEP** could also escape from **MNPs**; however, its release rate was slower than that of **cPt** under the same conditions, possibly resulting from its relatively low diffusion ability (SI Appendix, Fig. S18). These studies demonstrated that the chemotherapeutic drug and photosensitizer could be released in lysosomes/endosomes, predicting that the photochemotherapy may synergistically work inside cancer cells.

The cellular internalization of **MNPs** was studied using confocal microscopy (CLSM) and ICP-MS. As shown in Fig. 3B, a red fluorescence of **OEP** was observed in cytoplasm after the cells were incubated with **MNPs** for 8 h. The intracellular red fluorescence was greatly weakened by pretreating A2780CIS cells with free cRGDFK (SI Appendix, Fig. S19), demonstrating that the existence of targeting ligands on the surface of **MNPs** was favorable for their receptor-mediated uptake. ICP-MS results further indicated that the uptake of **MNPs** by A2780CIS cells was time-dependent (Fig. 3D); the intracellular platinum content increased by extending the incubation time. For example, the intracellular platinum content increased from 56.8 to 135 ng Pt/mg protein when the incubation time was extended from 1 to 4 h. Similarly, the internalization of **MNPs** was blocked when the receptors were occupied by pretreating the cells with free cRGDFK. The intracellular Pt content in A2780CIS cells cultured with NPs formed from **M $\Delta$ OEP** and **N<sub>3</sub>-PEG-*b*-PLBG**, i.e., without including the targeting groups, was much lower than that of **MNPs** under the same conditions, further confirming that the presence of targeting ligands facilitated the cellular internalization of **MNPs**.

Singlet oxygen sensor green (SOSG), a highly selective  $^1\text{O}_2$  probe, was utilized to detect the generation of  $^1\text{O}_2$  by **MNPs** upon laser irradiation of a solution containing **SOSG** and **MNPs**. The characteristic peak at 532 nm rapidly increased (Fig. 4A), because the **SOSG** in silent form was oxidized by the generated  $^1\text{O}_2$ . Likewise, in the UV-vis spectrum of a solution containing

anthracene-9,10-dipropionic acid disodium (ADPA) and **MNPs**, all of the diagnostic absorption bands (340–450 nm) of ADPA were gradually decreased upon irradiation, which confirmed the oxidation of ADPA by  $^1\text{O}_2$  (Fig. 4B). In contrast, negligible changes in ADPA's absorptions were noticed when **OEP** was employed as a photosensitizer, suggesting that the aggregation of **OEP** in aqueous solution was responsible for this negative outcome (SI Appendix, Figs. S20 and S21). This difference emphasized that the host-guest complexation and nanoformulation greatly improved the photodynamic effect of **OEP**. The intracellular  $^1\text{O}_2$  generation by **MNPs** was evaluated using dichlorofluorescein diacetate (DCF-DA) as an oxidant-sensitive fluorescent dye, which was nonfluorescent in its original state but became highly emissive after being oxidized into dichlorofluorescein (DCF). CLSM images showed that the strong green fluorescence of DCF was observed in the cytoplasm of A2780CIS cells cultured with **MNPs** followed by irradiation, a direct evidence for the efficient generation of  $^1\text{O}_2$  inside the cells (Fig. 4G and H). In a control experiment, vitamin C was employed as a  $^1\text{O}_2$  scavenger that could deplete the intracellular  $^1\text{O}_2$  originating from the photodynamic effect. Fig. 4I indicated that the green fluorescence significantly diminished by pretreating the cells with vitamin C (50.0  $\mu\text{M}$ ), further confirming the effective  $^1\text{O}_2$  production by **MNPs** under laser irradiation. Flow cytometry was also utilized to monitor the intracellular generation and scavenging of  $^1\text{O}_2$  by probing the green fluorescence of DCF (Fig. 4J–L); the data were in good agreement with the CLSM images.

A 3-(4',5'-dimethylthiazol-2'-yl)-2,5-diphenyl tetrazolium bromide (MTT) assay was used to assess the synergistic anticancer efficacy of the photochemotherapy. Cisplatin and **OEP**-loaded NPs (**PNPs**) were used as controls for the chemotherapy and PDT, respectively. For A2780 cells, the  $\text{IC}_{50}$  values of cisplatin, **cPt**, **MNPs**, and **PNPs**, followed by laser irradiation (**PNPs** + L), and **MNPs**, followed by irradiation (**MNPs** + L) were measured to be  $2.53 \pm 0.16$ ,  $3.57 \pm 0.28$ ,  $1.32 \pm 0.10$ ,  $1.05 \pm 0.08$ , and  $0.39 \pm 0.04$   $\mu\text{M}$ , respectively (Fig. 4C). The combination index (CI) was calculated to be 0.67, which was lower than 1, indicating a synergistic effect was realized for the **MNPs** by combining PDT and chemotherapy. Due to the drug resistance, the  $\text{IC}_{50}$  values against

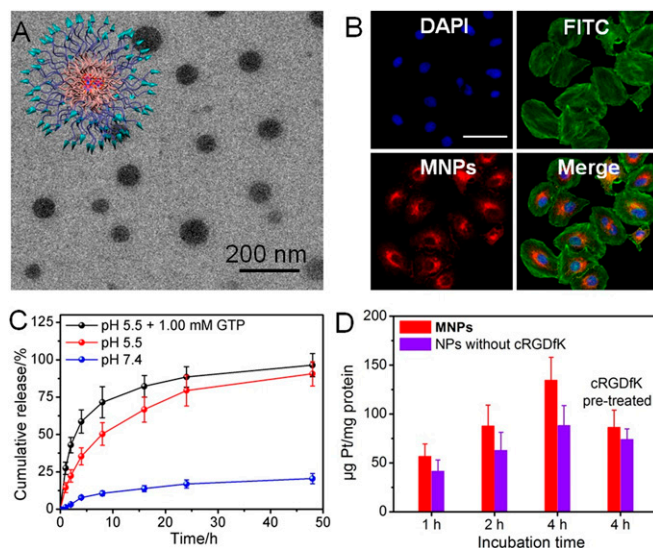


**Fig. 3.** (A) TEM image of **MNPs**. (B) CLSM image of A2780CIS cells treated with **MNPs**. Blue fluorescence is from the nucleus stained with DAPI, green fluorescence is from the  $\beta$ -actin stained with FITC, and red fluorescence is from **MNPs**. (Scale bars: 25  $\mu\text{m}$ .) (C) Release behaviors of the platinum-based drug under different conditions. (D) Time-dependent internalization of **MNPs** or NPs without cRGDFK by A2780CIS cells.

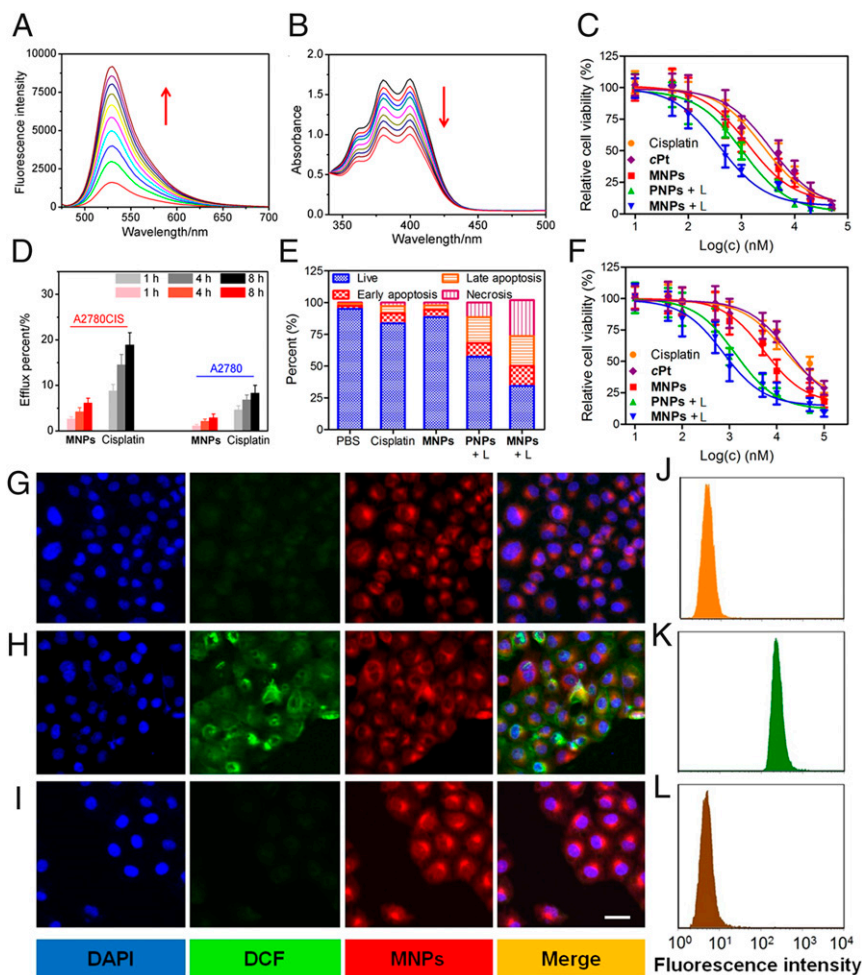


**Fig. 4.** (A) The fluorescence spectra of SOSG solution (5.00  $\mu\text{M}$ ) in the presence of **MNPs** upon irradiation for different time. (B) UV-vis spectra of APDA in the presence of **MNPs** upon light irradiation for different time. (C) Cytotoxicity of different formulations against A2780 cells. (D) Efflux percentage of cisplatin and **cPt** from A2780 and A2780CIS cells after different incubation time. (E) Annexin-V/PI analyses of A2780CIS cells after different treatments. (F) Cytotoxicity of different formulations against A2780CIS cells. (G–L) CLSM images (G–I) and flow cytometric analysis (J–L) of A2780CIS cells after incubation with **MNPs** and DCF-DA with irradiation for 0 min (G–J), 5 min (H and K), and 5 min (I and L) in the presence of vitamin C (50.0  $\mu\text{M}$ ).

cisplatin-resistant A2780CIS cells were increased to  $13.8 \pm 1.22$ ,  $18.6 \pm 1.59$ , and  $5.42 \pm 0.71$   $\mu\text{M}$  for cisplatin, **cPt**, and **MNPs**, respectively, indicating that a single chemotherapy was ineffective (Fig. 4F). Drug efflux was one of the possible reasons for the inactivation of chemotherapy against A2780CIS cells (33–35). Compared with A2780 cells, more drugs were pumped out from A2780CIS cells for both free cisplatin and **MNPs** (Fig. 4D). Interestingly, nanoformulation was favorable to inhibit drug efflux, as indicated by the lower Pt amount in the culture medium than that of cisplatin. For **PNPs + L**, the  $\text{IC}_{50}$  values against A2780CIS ( $1.37 \pm 0.21$   $\mu\text{M}$ ) and A2780 cell lines were comparable because of the different anticancer mechanism between chemotherapy and PDT. The most promising results were observed from the cells treated with **MNPs + L**; the cytotoxicity toward the A2780CIS cell was improved, yielding an  $\text{IC}_{50}$  value of  $0.76 \pm 0.09$   $\mu\text{M}$ . The enhanced anticancer efficacy was attributed to the synergistic effect of chemotherapy and PDT as evidenced by the CI value of 0.69.

Annexin-V FITC/propidium iodide (PI) dual-staining provided further insight into the anticancer efficacy by quantitatively distinguishing the cells in the apoptotic/necrotic status after different administrations (Fig. 4E). For chemotherapy alone (cisplatin and **MNPs**), only a small quantity of apoptotic and necrotic cells were detected arising from their low anticancer activity, while the apoptotic/necrotic population increased to

42.7% for the A2780CIS cells treated with **PNPs + L** (i.e., PDT). In contrast, the photochemotherapy (**MNPs + L**) evoked the highest level of apoptosis (39.3%) and necrosis (28.4%) among these formulations due to its superior anticancer efficacy. In vitro anticancer experiments confirmed that the combination of PDT and chemotherapy resulted in a synergistically enhanced therapeutic outcome that can overcome drug resistance.

The blood circulation and tumor accumulation of **MNPs** were evaluated using ICP-MS and fluorescence imaging. The pharmacokinetic profile of **MNPs** was obtained by determining the amount of Pt in the blood after different time postinjection using ICP-MS (SI Appendix, Fig. S22). Cisplatin was used as a control that was rapidly cleared from the blood, and its circulation half-life was calculated to be  $0.33 \pm 0.05$  h. Benefiting from the EPR effect and active targeting ability, the circulation half-life of **MNPs** was prolonged to  $1.87 \pm 0.24$  h, which was 5.7-fold higher than that of free cisplatin.

Since **OEP** is also a NIR fluorophore, a whole-body fluorescence imaging study was conducted to monitor the delivery of **MNPs** after i.v. injection. As shown in Fig. 5A, a significant amount of **MNPs** accumulated in the tumor area at 6 h postinjection, and the fluorescence signals were progressively strengthened at 12 and 24 h postinjection, indicating that **MNPs** possessed high tumor accumulation and retention capabilities. Furthermore, the time-dependent

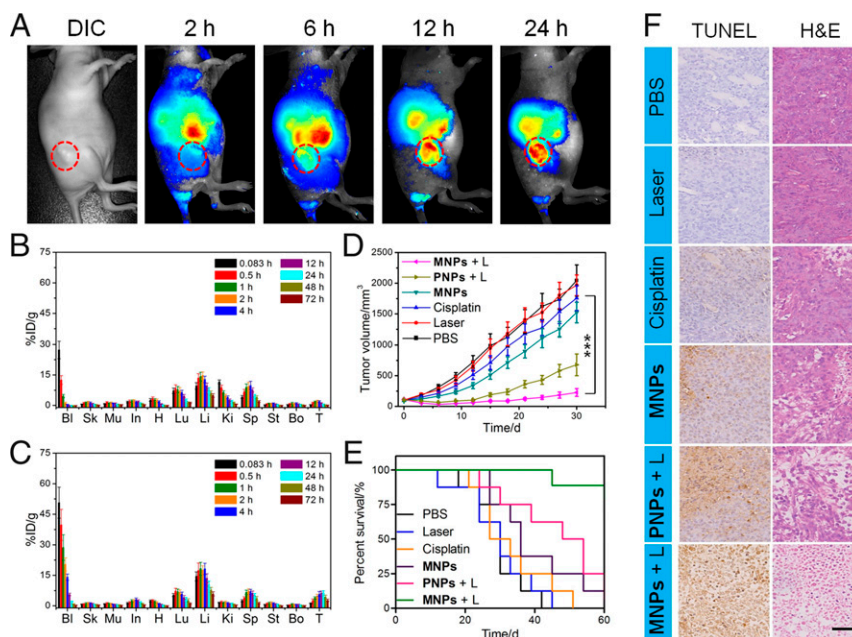


**Fig. 5.** (A) Time-dependent fluorescence images of A2780CIS tumor-bearing mouse after i.v. injection of MNPs. Tissue distributions of cisplatin (B) and MNPs (C) at different time post-i.v. injection. Bl, blood; Bo, bone; H, heart; In, intestine; K, kidney; Li, liver; Lu, lung; Mu, muscle; Sk, skin; Sp, spleen; St, stomach; T, tumor. (D and E) Tumor growth inhibition curves (D) and survival rate (E) of the mice bearing A2780CIS tumors after different treatments ( $n = 8$ ).  $***P < 0.001$ . (F) TUNEL and H&E staining of the tumor tissues from the mice treated with different formulations. (Scale bar: 200  $\mu\text{m}$ .)

biodistribution of MNPs in the main organs and tumors was quantitatively analyzed by ICP-MS. As a low-molecular-weight drug, cisplatin entered the organs rapidly; the maximum platinum level in each organ was observed within 2 h after i.v. injection (Fig. 5B). Due to its fast clearance, the platinum amount accumulated in the tumor tissues was low, the highest platinum concentration in the tumor was  $1.93 \pm 0.34\% \text{ID/g}$  (percentage injected dose/gram tissue) at 2 h postinjection. It should be noted that the drug was eliminated from the body mainly through a renal excretion pathway. This was supported by the fact that a high platinum level was monitored in the kidney at the first 2 h, which was likely responsible for its severe nephrotoxicity. For the mice treated with MNPs, the Pt amount in the tumor gradually increased to  $6.47 \pm 0.92\% \text{ID/g}$  at 24 h postinjection (Fig. 5C), which was 10.8-fold higher than that of the cisplatin-treated group ( $0.60 \pm 0.09\% \text{ID/g}$ ). The intratumoral platinum level was maintained at a relatively high level ( $2.73 \pm 0.41\% \text{ID/g}$ ) even after 72 h postinjection. Due to the prolonged blood circulation time, a high accumulation of MNPs was monitored in the reticuloendothelial system, such as the liver and spleen, which was common in most nanomedicines. Additionally, the employment of nanoparticles as drug-delivery carriers reduced the platinum level in the kidney, greatly avoiding the renal toxicity of platinum-based anticancer drugs.

The in vivo antitumor performance of the photochemotherapy was evaluated using A2780CIS tumor-bearing nude mice. As shown in Fig. 5D, no influence on the tumor growth was observed by the laser irradiation, as verified by the tumors' rapid growth. Compared with the control group administrated with PBS, limited therapeutic results were observed for the mice that received a single chemotherapy (cisplatin and MNPs), because the drug-resistant tumor model was insensitive to chemotherapy. Due to the EPR effect and targeting capability, a relatively higher antitumor efficacy was realized for the mice treated with MNPs than those administrated with cisplatin. For PDT alone (PNPs + L), an effective tumor growth inhibition was achieved in the first 12 d. However, a tumor recurrence appeared afterward, because the infiltrating cancer cells far away from the primary tumor were hardly cleared by a single PDT. The inhibition ratio was calculated to be 14.1%, 25.5%, and 66.8% for the

mice administrated with cisplatin, MNPs, and PNPs + L, respectively (SI Appendix, Fig. S23). A superior antitumor outcome was achieved for the mice receiving photochemotherapy, in which the tumor inhibition rate reached 89.2%. H&E staining demonstrated that the photochemotherapy caused the highest level of apoptosis and necrosis in tumor tissues (Fig. 5F). Furthermore, TUNEL staining showed that photochemotherapy resulted in 93.8% cell apoptosis in tumor sites, which was much higher than the other formulations (Fig. 5F and SI Appendix, Fig. S24), thereby confirming the synergistic anticancer efficacy of MNPs.

During the therapeutic period, the changes in body weight were monitored to assess the systemic toxicity of each formulation. Due to the nonspecific distribution of cisplatin, the administration led to a serious weight loss after three injections (SI Appendix, Fig. S25). The systemic toxicity of cPt was greatly avoided by incorporating the drug into the nanomedicine. Negligible body weight reduction was observed during the therapy period for the mice treated with MNPs or MNPs + L. Moreover, no obvious signs of toxic effects, such as eating, drinking, activity, grooming, urination, or neurological status occurred. The low toxicity of MNPs + L was further evaluated by H&E staining of the main organs (SI Appendix, Fig. S26), in which no observable inflammatory lesions and tissue damages were detected. The median survival rate of the mice treated with PBS, laser, cisplatin, MNPs, and PNPs + L was determined to be 28, 29, 31, 36, and 51 d, respectively, whereas the survival rate extended over 60 d for the mice that received photochemotherapy (Fig. 5E). Moreover, in vivo blood biochemistry test demonstrated that the hepatotoxicity and nephrotoxicity of the platinum-based anticancer drug were significantly inhibited through nanoformulations (SI Appendix, Fig. S27). Routine blood analysis indicated that the levels of the biomarkers were in the normal range (SI Appendix, Fig. S28), and a negligible difference was found between the healthy mice and the mice treated with photochemotherapy.

## Conclusion

In summary, a discrete organoplatinum(II) metallacage **M** containing a platinum-based anticancer drug was employed to encapsulate a photosensitizer (OEP) through noncovalent interactions. The

host-guest complex was further wrapped up by an amphiphilic copolymer, resulting in the formation of MNPs with the capability to codeliver a chemotherapeutic agent and a photosensitizer. The targeting ligand was introduced through an in situ copper-free click reaction, endowing the formed MNPs with the ability to specifically deliver cPt and OEP to cancer cells overexpressing  $\alpha_v\beta_3$  integrin. The MNPs were highly accumulated in the tumor sites benefiting from the EPR effect and active targeting, which were favorable to enhance the therapeutic outcome and reduce side effects. In vivo studies demonstrated that MNPs exhibited a superior antitumor performance on a drug-resistant tumor model by combining chemotherapy and PDT. This work demonstrates a strategy for delivering multiple therapeutic agents/diagnostic probes through supramolecular chemistry that can be useful in treating many difficult-to-treat cancers including drug resistance and thereby possessing promising potentials in cancer theranostics.

## Materials and Methods

Azide-PEG-amine ( $N_3$ -PEG- $NH_2$ , 2k) was purchased from Biochempeg. Triphosgene, L-glutamic acid,  $\gamma$ -benzyl ester, and other reagents were purchased from Sigma-Aldrich and used as received. Solvents were either employed as purchased or dried according to procedures described in the literature.  $^1H$  NMR and  $^{31}P$  NMR spectra were recorded on a Bruker Avance

III-300 or 400 spectrometer.  $^{31}P\{^1H\}$  NMR chemical shifts are referenced to an external unlocked sample of 85%  $H_3PO_4$ . UV-vis spectra were taken on a Shimadzu UV-3150 spectrophotometer. TEM investigations were carried out on a Hitachi HT7700 instrument. The fluorescence experiments were conducted on a RF-5301 spectrofluorophotometer (Shimadzu Corporation). DLS measurements were carried out using a 200-mW polarized laser source Nd:YAG ( $\lambda = 532$  nm). The polarized scattered light was collected at  $90^\circ$  in a self-beating mode with a Hamamatsu R942/02 photomultiplier. The signals were sent to a Malvern 4700 submicrometer particle analyzer system. Molecular weights and distributions were determined by gel permeation chromatography with a Waters 1515 pump and Waters 1515 differential refractive index detector (set at  $30^\circ C$ ).

All experiments involving live animals were approved by the Zhejiang University Animal Care and Use Committee. The details of the synthesis and characterization are given in *SI Appendix*.

**ACKNOWLEDGMENTS.** This work was supported by the Intramural Research Program of the National Institute of Biomedical Imaging and Bioengineering, NIH (to X.C.), NIH Grant R01 CA215157 (to P.J.S.), National Natural Science Foundation of China Grants 21572042 and 21773052 (to S.L.), Program for Innovative Research Team in Chinese University Grant IRT1231 (to S.L.), Zhejiang Provincial Natural Science Foundation of China Grant LZ16B020002 (to S.L.), and Program for Hangzhou Social Development of China Grant 20170533B10 (to S.L.).

- Johnstone TC, Suntharalingam K, Lippard SJ (2016) The next generation of platinum drugs: Targeted Pt(II) agents, nanoparticle delivery, and Pt(IV) prodrugs. *Chem Rev* 116:3436–3486.
- Wang D, Lippard SJ (2005) Cellular processing of platinum anticancer drugs. *Nat Rev Drug Discov* 4:307–320.
- Cook TR, Vajpayee V, Lee MH, Stang PJ, Chi KW (2013) Biomedical and biochemical applications of self-assembled metallacycles and metallacages. *Acc Chem Res* 46:2464–2474.
- Liu HK, Sadler PJ (2011) Metal complexes as DNA intercalators. *Acc Chem Res* 44:349–359.
- Kelland L (2007) The resurgence of platinum-based cancer chemotherapy. *Nat Rev Cancer* 7:573–584.
- Oun R, Moussa YE, Wheate NJ (2018) The side effects of platinum-based chemotherapy drugs: A review for chemists. *Dalton Trans* 47:6645–6653.
- Wang X, Wang X, Guo Z (2015) Functionalization of platinum complexes for biomedical applications. *Acc Chem Res* 48:2622–2631.
- Miller MA, et al. (2015) Tumour-associated macrophages act as a slow-release reservoir of nano-therapeutic Pt(IV) pro-drug. *Nat Commun* 6:8692.
- Browning RJ, et al. (2017) Drug delivery strategies for platinum-based chemotherapy. *ACS Nano* 11:8560–8578.
- Wang X, Guo Z (2013) Targeting and delivery of platinum-based anticancer drugs. *Chem Soc Rev* 42:202–224.
- Wilson JJ, Lippard SJ (2014) Synthetic methods for the preparation of platinum anticancer complexes. *Chem Rev* 114:4470–4495.
- Yu G, et al. (2018) A discrete organoplatinum(II) metallacage as a multimodality theranostic platform for cancer photochemotherapy. *Nat Commun* 9:4335.
- Naik A, Rubbiani R, Gasser G, Spingler B (2014) Visible-light-induced annihilation of tumor cells with platinum-porphyrin conjugates. *Angew Chem Int Ed Engl* 53:6938–6941.
- Harrington KJ, et al. (2000) Pegylated liposome-encapsulated doxorubicin and cisplatin enhance the effect of radiotherapy in a tumor xenograft model. *Clin Cancer Res* 6:4939–4949.
- He C, Poon C, Chan C, Yamada SD, Lin W (2016) Nanoscale coordination polymers codeliver chemotherapeutics and siRNAs to eradicate tumors of cisplatin-resistant ovarian cancer. *J Am Chem Soc* 138:6010–6019.
- Ng KK, Zheng G (2015) Molecular interactions in organic nanoparticles for photo-theranostic applications. *Chem Rev* 115:11012–11042.
- Ethirajan M, Chen Y, Joshi P, Pandey RK (2011) The role of porphyrin chemistry in tumor imaging and photodynamic therapy. *Chem Soc Rev* 40:340–362.
- Lucky SS, Soo KC, Zhang Y (2015) Nanoparticles in photodynamic therapy. *Chem Rev* 115:1990–2042.
- He C, Liu D, Lin W (2015) Self-assembled core-shell nanoparticles for combined chemotherapy and photodynamic therapy of resistant head and neck cancers. *ACS Nano* 9:991–1003.
- Chen W, et al. (2017) Black phosphorus nanosheet-based drug delivery system for synergistic photodynamic/photothermal/chemotherapy of cancer. *Adv Mater* 29:1603864.
- Fan F, Wang L, Li F, Fu Y, Xu H (2016) Stimuli-responsive layer-by-layer tellurium-containing polymer films for the combination of chemotherapy and photodynamic therapy. *ACS Appl Mater Interfaces* 8:17004–17010.
- Yuan Y, Liu J, Liu B (2014) Conjugated-polyelectrolyte-based polyprodrug: Targeted and image-guided photodynamic and chemotherapy with on-demand drug release upon irradiation with a single light source. *Angew Chem Int Ed Engl* 53:7163–7168.
- Park W, et al. (2016) Intermolecular structural change for thermoswitchable polymeric photosensitizer. *J Am Chem Soc* 138:10734–10737.
- Li Y, et al. (2014) A smart and versatile theranostic nanomedicine platform based on nanoporphyrin. *Nat Commun* 5:4712.
- Wang M, Zheng YR, Ghosh K, Stang PJ (2010) Metallosupramolecular tetragonal prisms via multicomponent coordination-driven template-free self-assembly. *J Am Chem Soc* 132:6282–6283.
- Yu G, et al. (2016) Tetraphenylethene-based highly emissive metallacage as a component of theranostic supramolecular nanoparticles. *Proc Natl Acad Sci USA* 113:13720–13725.
- Chen LJ, Yang HB (2018) Construction of stimuli-responsive functional materials via hierarchical self-assembly involving coordination interactions. *Acc Chem Res* 51:2699–2710.
- Zhang M, et al. (2017) Multicomponent platinum(II) cages with tunable emission and amino acid sensing. *J Am Chem Soc* 139:5067–5074.
- Knop K, Hoogenboom R, Fischer D, Schubert US (2010) Poly(ethylene glycol) in drug delivery: Pros and cons as well as potential alternatives. *Angew Chem Int Ed Engl* 49:6288–6308.
- Schöttler S, et al. (2016) Protein adsorption is required for stealth effect of poly(ethylene glycol)- and poly(phosphoester)-coated nanocarriers. *Nat Nanotechnol* 11:372–377.
- Yu G, et al. (2017) Antitumor activity of a unique polymer that incorporates a fluorescent self-assembled metallacycle. *J Am Chem Soc* 139:15940–15949.
- Fuertes MA, Alonso C, Pérez JM (2003) Biochemical modulation of cisplatin mechanisms of action: Enhancement of antitumor activity and circumvention of drug resistance. *Chem Rev* 103:645–662.
- Szakács G, Paterson JK, Ludwig JA, Booth-Genthe C, Gottesman MM (2006) Targeting multidrug resistance in cancer. *Nat Rev Drug Discov* 5:219–234.
- Ling X, et al. (2018) Glutathione-scavenging poly(disulfide amide) nanoparticles for the effective delivery of Pt(IV) prodrugs and reversal of cisplatin resistance. *Nano Lett* 18:4618–4625.
- Li Y, et al. (2015) Multipronged design of light-triggered nanoparticles to overcome cisplatin resistance for efficient ablation of resistant tumor. *ACS Nano* 9:9626–9637.